Supporting Information

3D High-Density MXene@MnO_2 Microflowers for Advanced Aqueous Zinc-Ion Batteries

Minjie Shi[a#], Bei Wang[a#], Cong Chen[a], Junwei Lang[c], Chao Yan[a] and Xingbin Yan[b,c]**

[a] *School of Materials Science and Engineering, Jiangsu University of Science and Technology, Zhenjiang, 212003, P. R. China*

[b] *State Key Laboratory of Optoelectronic Materials and Technologies, School of Materials Science and Engineering, Sun Yat-Sen University, Guangzhou, 510275, P. R. China*

[c] *Laboratory of Clean Energy Chemistry and Materials, Lanzhou Institute of Chemical Physics, Chinese Academy of Sciences, Lanzhou, 730000, P. R. China*

* *Corresponding author*

E-mail address: xbyan@licp.cas.cn (X. B. Yan); chaoyan@just.edu.cn (C. Yan).

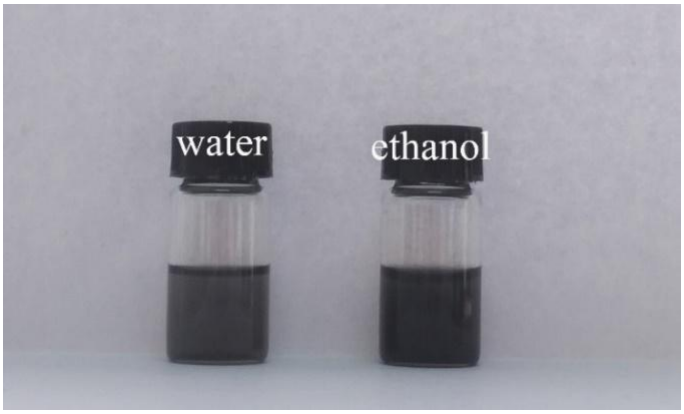

Fig. S1. Digital photo of the distribution of $Ti_3C_2T_x$ nanosheets (1.0 mg mL^{-1}) in water and ethanol solution.

As shown in the Fig. S1, it is found that $Ti_3C_2T_x$ nanosheets can be uniformly dispersed in the common solvents (especially water and ethanol) by hand shaking and kept stable for a long time, which is mainly owing to the sufficient functional groups of $Ti_3C_2T_x$ nanosheets that ensure their good hydrophilic surfaces.

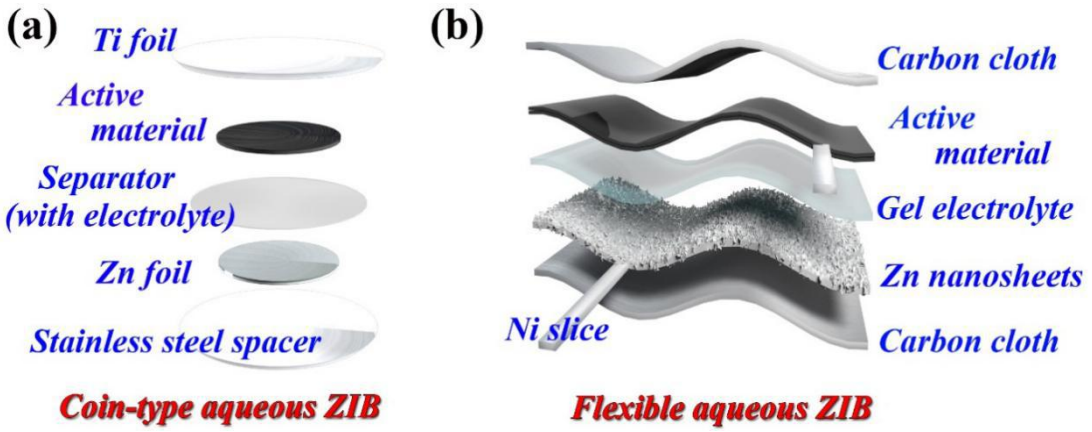

Fig. S2. Schematic diagrams of the fabrication of (a) coin-type and (b) flexible aqueous ZIBs.

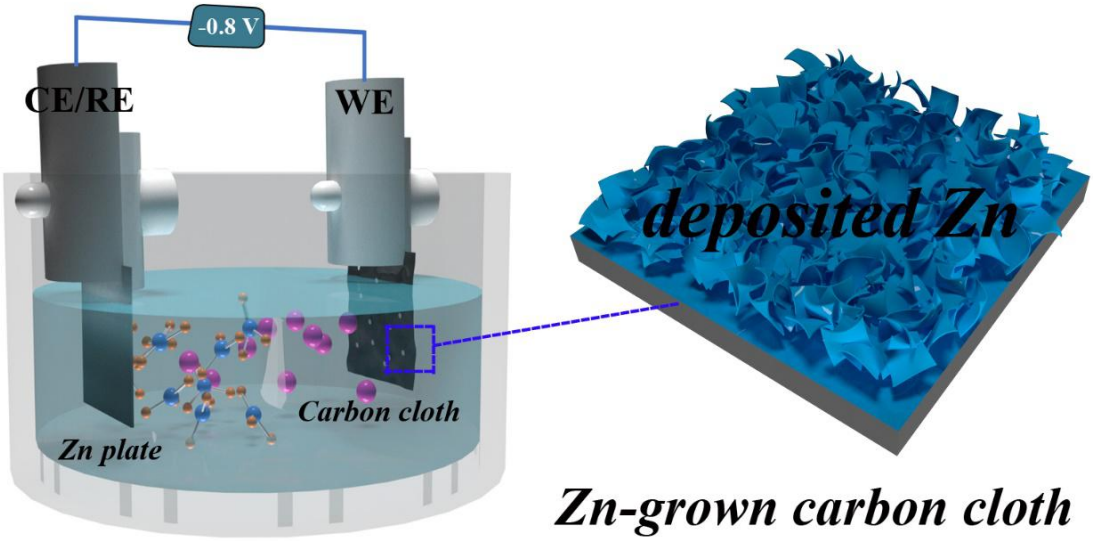

Fig. S3. Schematic diagram of potentiostatic electrodeposition for the deposition of Zn on carbon cloth.

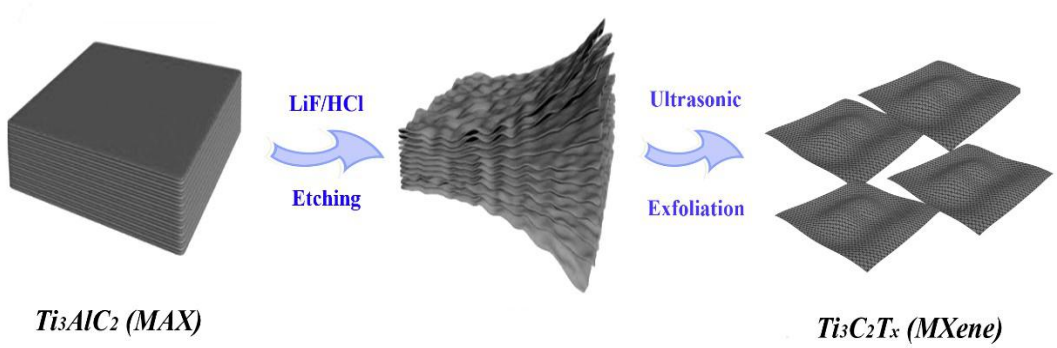

Fig. S4. Schematic diagram of the preparation process of ultrathin $Ti_3C_2T_x$ nanosheets.

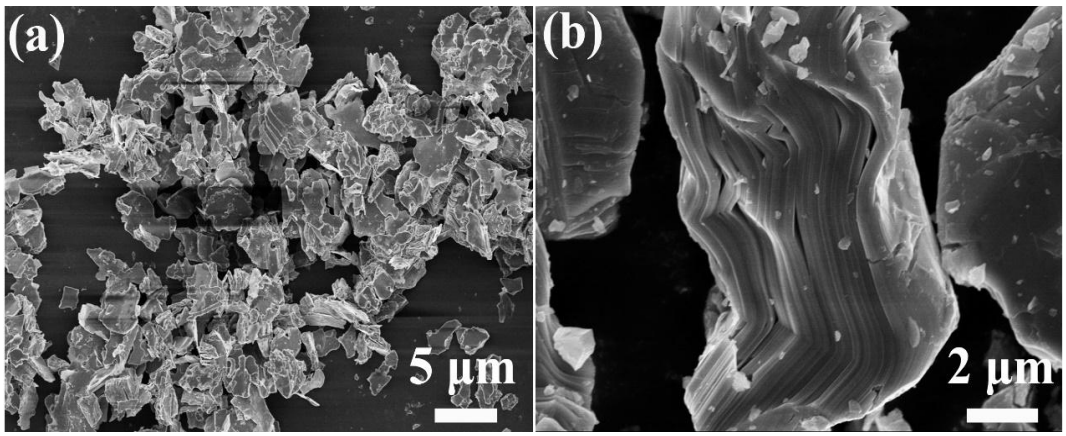

Fig. S5. SEM images of MAX phase (Ti_3AlC_2).

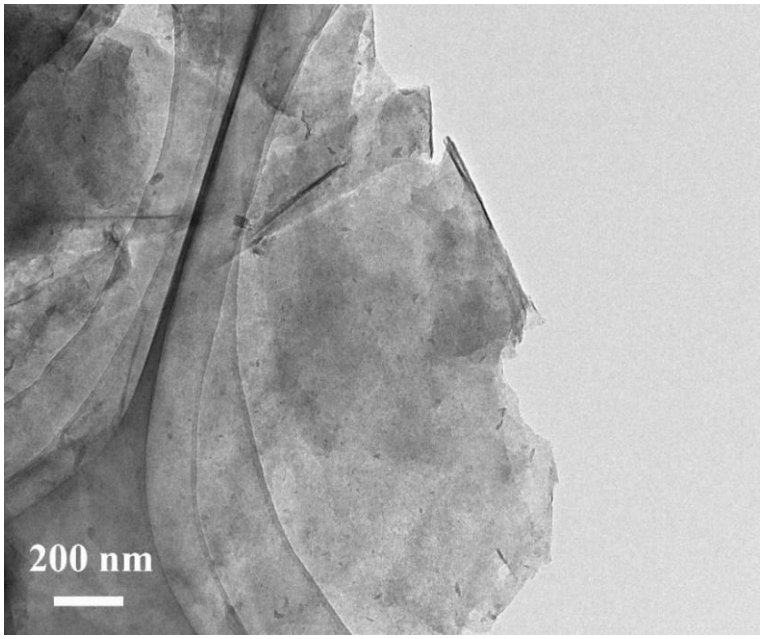

Fig. S6. A typical TEM image of ultrathin $Ti_3C_2T_x$ nanosheets.

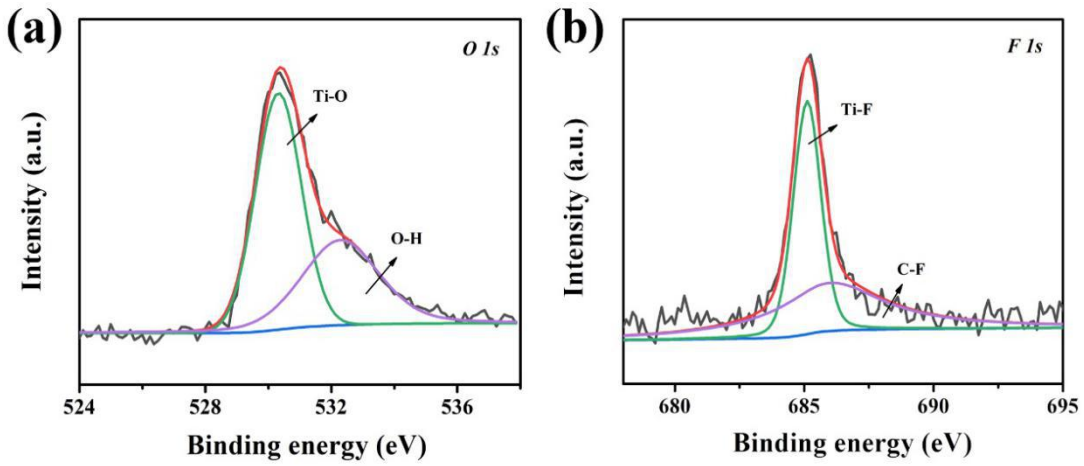

Fig. S7. (a) O 1s and (b) F 1s high-resolution XPS spectra of $Ti_3C_2T_x$ nanosheets.

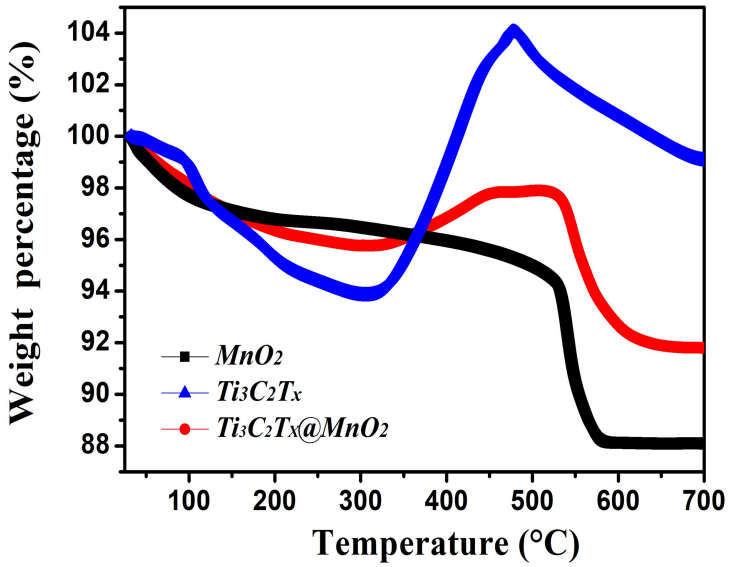

Fig. S8. TGA curves of MnO_2, $Ti_3C_2T_x$ and 3D $Ti_3C_2T_x$@MnO_2 microflowers under air atmosphere.

Fig. S8 shows the TGA curves of MnO_2, $Ti_3C_2T_x$ and 3D $Ti_3C_2T_x$@MnO_2 microflowers at the heating rate of 10 °C min^{-1} in air atmosphere. Obviously, MnO_2 shows the thermal stability with the weight percentage of 89.1% at 700 °C (black curve). Unlike MnO_2, the weight of the $Ti_3C_2T_x$ exhibits an obvious rise at the temperature ranging from 300 to 470 °C, which can be explained by the oxidation of $Ti_3C_2T_x$ in air atmosphere.[1, 2] As for 3D $Ti_3C_2T_x$@MnO_2 microflowers, it is found that the weight percentage slowly rises as the temperature increases above 300 °C and finally drop to 91.8% at 700 °C (red curve). By calculating, the mass amount of $Ti_3C_2T_x$ in the 3D $Ti_3C_2T_x$@MnO_2 microflowers is determined as about 27.1%.

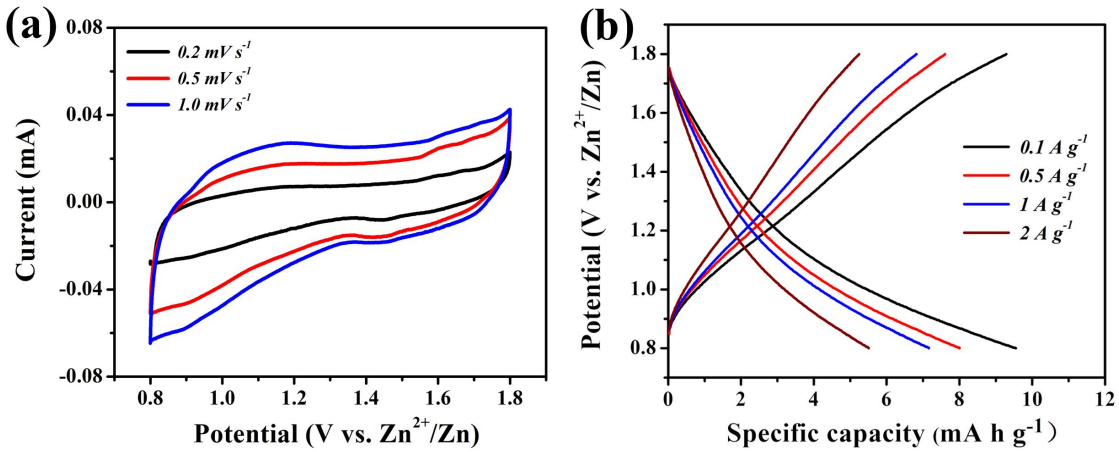

Fig. S9. (a) CV curves scanning at different rates and (b) GCD curves at various current densities of 3D $Ti_3C_2T_x$@RGO microspheres as cathode in aqueous ZIBs.

We have prepared 3D $Ti_3C_2T_x$@RGO microspheres cathode by using spray drying approach and tested its electrochemical behaviors in aqueous ZIBs. As shown in Fig. S9a, there are no obvious redox peaks in the curves of 3D $Ti_3C_2T_x$@RGO microspheres cathode, which is totally different from that of 3D $Ti_3C_2T_x$@MnO_2 microflowers cathode with two couples of obvious redox peaks (Fig. 3a). GCD curves (Fig. S9b) also indicate the inappreciable specific capacities (< 10 mAh g^{-1}) of 3D $Ti_3C_2T_x$@RGO microspheres cathode at different current densities in aqueous ZIBs, which is owing to the lack of obvious redox reaction and Zn^{2+} storage behaviors in the $Ti_3C_2T_x$@RGO microspheres cathode. Therefore, the advantages of 3D $Ti_3C_2T_x$@MnO_2 microflowers is the electro-active MnO_2 nanoparticles encapsulated in the crumpled and rippled $Ti_3C_2T_x$ nanosheets to form 3D microflowers, effectively providing the 3D $Ti_3C_2T_x$@MnO_2 microflowers with obvious Zn^{2+} storage behaviors and large specific capacity when compared to the 3D $Ti_3C_2T_x$@RGO microspheres.

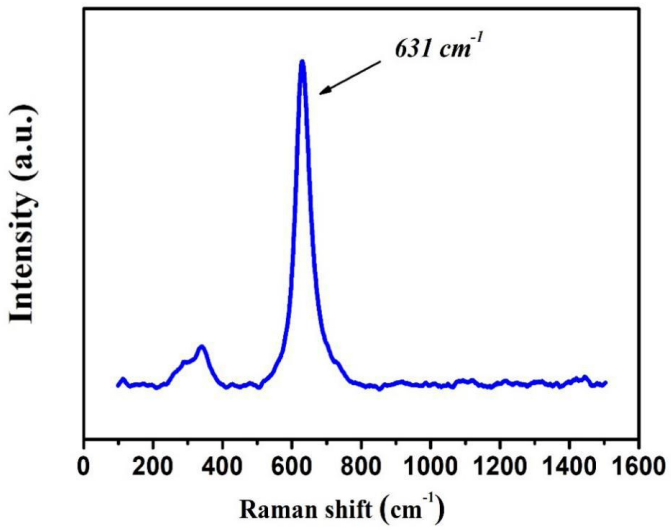

Fig. S10. Raman spectrum of 3D $Ti_3C_2T_x$@MnO_2 microflowers.

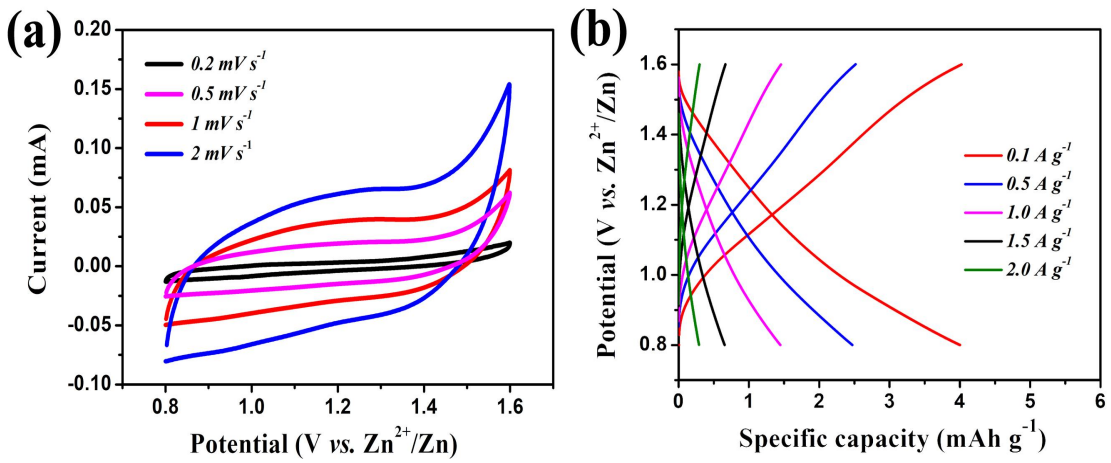

Fig. S11. (a) CV curves scanning at different rates and (b) GCD curves at various current densities of $Ti_3C_2T_x$ as cathode in aqueous ZIBs.

As we known, MnO_2 exists in a variety of crystallographic polymorphs, namely, α, β, γ, δ, and λ-type MnO_2. The fundamental unit in the crystal structure of MnO_2 polymorphs is composed of Mn^{4+} ions occupying octahedral holes formed by hexagonally close-packed oxide ions. Precisely, each Mn^{4+} ion is surrounded by six oxygen neighbors to form a fundamental MnO_6 octahedral unit. The realization of

MnO_2 polymorphs is dependent on the type of linkage between the fundamental octahedral units in the crystallographic structure.[3, 4] MnO_2 polymorphs possess tunnel-like structures that facilitate guest-ion insertion/deinsertion during electrochemical reactions. Among them, γ-MnO_2 phase comprised of randomly arranged 1 × 1 (size ~2.3 × 2.3 Å, pyrolusite) and 1 × 2 (size ~2.3 × 4.6 Å, ramsdellite) tunnel blocks exhibits considerable electrochemical behaviors in aqueous ZIBs, wherein the basic structural unit MnO_6 octahedra is connected to each other by coangle/co-edge, constructing chain, tunnel structures with enough space accommodating foreign cations, which are the key factors that affect the Zn^{2+} storage behaviors. In general, the stochastically distributed tunnel blocks of γ-MnO_2 are beneficial for the Zn^{2+} storage, which has been demonstrated by the previously reported γ-MnO_2 based cathodes for aqueous ZIBs.[5, 6] As shown in Fig. S11a, there are no redox peaks in the curves of $Ti_3C_2T_x$ cathode. GCD curves (Fig. S11b) also indicate the inappreciable specific capacities of $Ti_3C_2T_x$ cathode at different current densities in aqueous ZIBs. Although there are abundant functional groups (-O, -OH, and -F) on the surface of individual conductive flakes of $Ti_3C_2T_x$, these functional groups provide almost no Zn^{2+} storage behaviors for $Ti_3C_2T_x$ cathode upon Zn^{2+} insertion/extraction, which is owing to the lack of obvious redox reaction between Zn^{2+} and $Ti_3C_2T_x$ cathode. This result indicates that Zn^{2+} storage behaviors of 3D $Ti_3C_2T_x$@MnO_2 microflowers cathode are dominantly resulting from the reversible redox reaction of γ-phase MnO_2. During the early stages of Zn-insertion, it is highly probable that the 1 × 1 tunnel of the γ-MnO_2 mostly transform into the spinel-type phase.[7, 8] As the discharge reaction proceeds and further Zn-insertion, the 1 × 2 tunnels in the domains that retain the parent structure are occupied by Zn^{2+} ions, as well as their geometric dimension could be significantly expanded. During the later

stages of the discharge reaction as more Zn-insertion occurs, it is plausible that fully inserted tunnels could further expand and open up their structure,[7, 9] consequently resulting in the formation of layered-type birnessite ($ZnMn_2O_4$). On subsequent charging accompanied with Zn-deintercalation, the layered-type birnessite tends to become compressed, leading to the closing up of the structure to form original γ-phase MnO_2. Therefore, during the charging-discharging process, γ-MnO_2 could eventually form layered-type birnessite after phase transformation with the continuous Zn^{2+} intercalation, while this process is highly reversible since the Zn^{2+} extract from layered-type birnessite framework, resulting in the reinstatement of γ-MnO_2 upon Zn^{2+} de-intercalation.

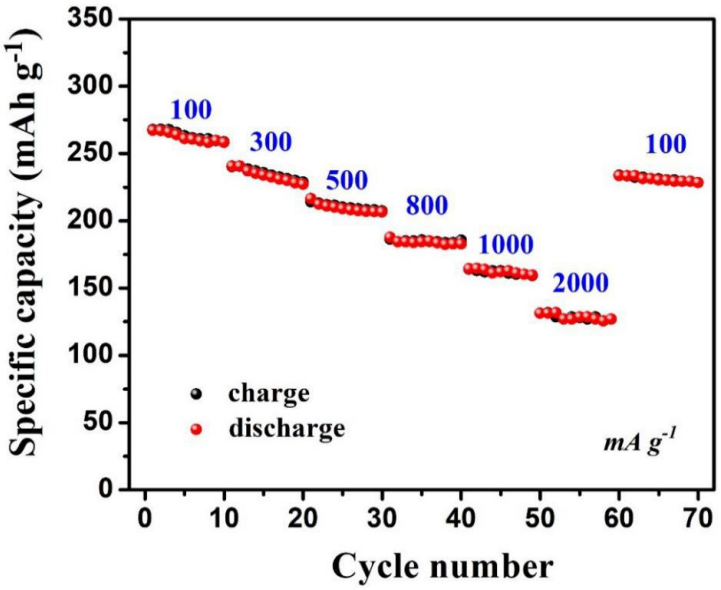

Fig. S12. Rate capability of pure MnO_2 as cathode in aqueous ZIBs at various current densities (100~2000 mA g^{-1}).

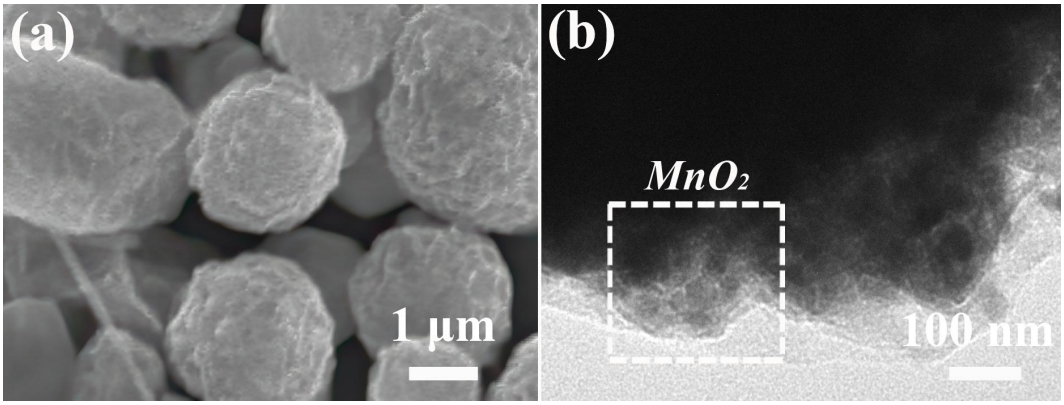

Fig. S13. (a) SEM and (b) TEM images of 3D $Ti_3C_2T_x$@MnO_2 microflowers cathode after cycles.

As shown in Fig. S13a, there is no obvious structural change and collapse of 3D architecture of the 3D $Ti_3C_2T_x$@MnO_2 microflowers cathode upon repeated Zn^{2+} insertion/extraction, in which MnO_2 nanoparticles without serious aggregation are still encapsulated in the crumpled and rippled $Ti_3C_2T_x$ nanosheets after cycles (Fig. S13b). The effective integration of electro-active MnO_2 with $Ti_3C_2T_x$ nanosheets to form a robust 3D microflower-like structure can greatly inhibit the dissolution and aggregation of MnO_2 nanoparticles during repeated charging-discharging processes, thereby rendering the high cycling stability of the 3D $Ti_3C_2T_x$@MnO_2 microflowers cathode in aqueous ZIBs.

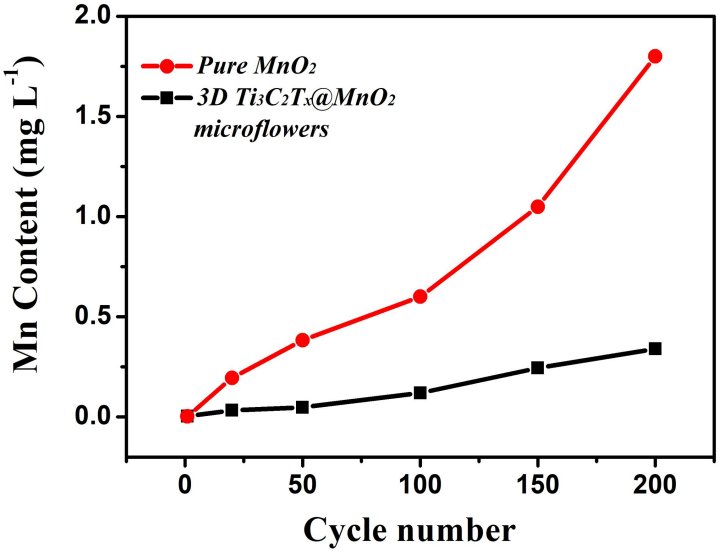

Fig. S14. Element analysis of dissolved Mn content in 2 M $ZnSO_4$ aqueous electrolyte during cycles of pure MnO_2 and 3D $Ti_3C_2T_x$@MnO_2 microflowers cathodes.

Mn dissolution has been regarded a major issue for the structure degradation of MnO_2-based cathodes that results in the impedance rise and capacity fading of aqeoues ZIBs during cycles.[10, 11] ICP analysis have been introduced to measure the dissolved Mn content in 2 M $ZnSO_4$ aqeoues electrolyte for pure MnO_2 and 3D $Ti_3C_2T_x$@MnO_2 microflowers cathodes during cycles. As shown in Fig.S14, it is found that pure MnO_2 cathode without microflower-like structure exhibits a fast Mn dissolution and the content of Mn dissolution in the electrolyte is significantly increasing during cycles. By constrat, 3D $Ti_3C_2T_x$@MnO_2 microflowers cathode shows a stable dissolved Mn content in 2 M $ZnSO_4$ aqeoues electrolyte after 200 cycles. The level of dissolved Mn in the electrolyte is much lower than that for pure MnO_2 cathode, indicating the Mn dissolution could be effectively alleviated in 3D $Ti_3C_2T_x$@MnO_2 microflowers cathode.

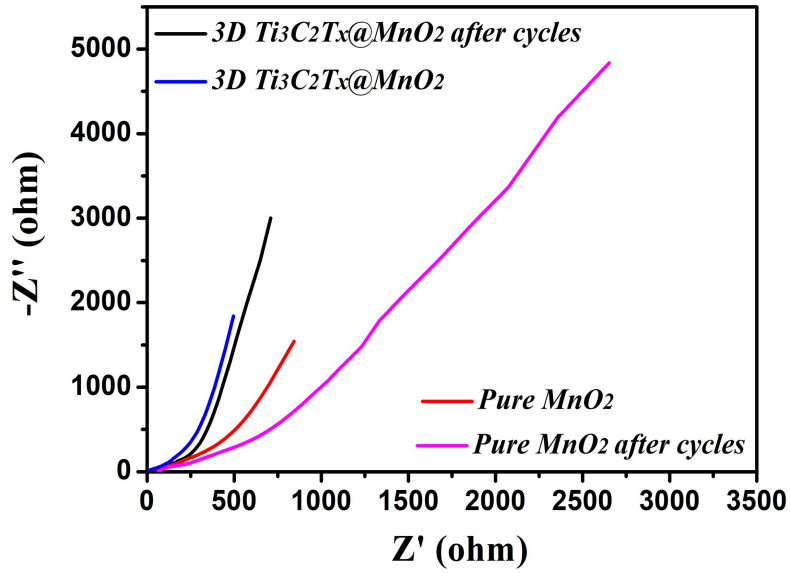

Fig. S15. EIS plots of pure MnO_2 and 3D $Ti_3C_2T_x$@MnO_2 microflowers cathodes before and after 1000 cycles in aqeoues ZIBs.

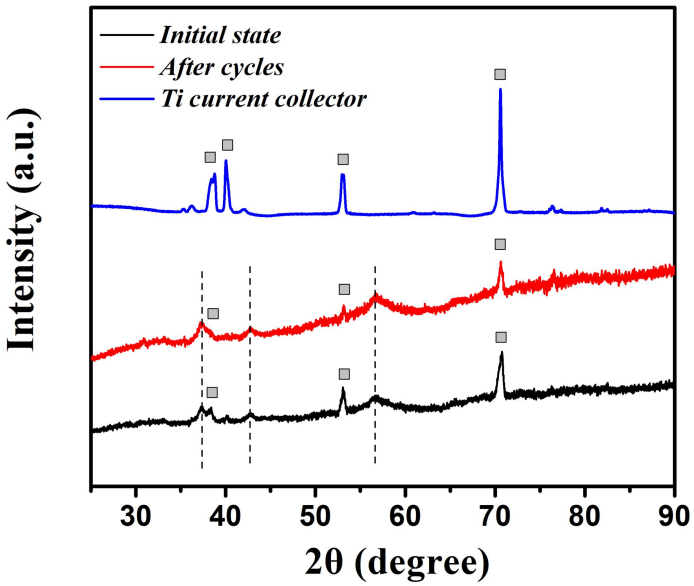

Fig. S16. XRD patterns of 3D $Ti_3C_2T_x$@MnO_2 microflowers cathode before and after 1000 cycles.

Fig. S15 shows the EIS plots of pure MnO_2 and 3D $Ti_3C_2T_x$@MnO_2 microflowers cathodes before and after cycles. By contrast, there is no obvious variation of electrochemical kinetics of 3D $Ti_3C_2T_x$@MnO_2 microflowers cathode upon repeated

charging-discharging processes in aqueous ZIBs, indicating high structural sustainability of 3D $Ti_3C_2T_x$@MnO_2 microflowers cathode with efficient ions/electrons transfer during cycles. Additionally, the XRD analyses of 3D Ti_3C_2Tx@MnO_2 microflowers cathode before and after cycles were further carried out in aqueous ZIBs. As shown in Fig. S16, it can be clearly observed from the XRD pattern after cycles that the characteristic peaks of electro-active γ-MnO_2 still exist, while there is no other impurity peak when compared with the XRD pattern before the cycling test, suggesting that the highly reversible structural evolution of γ-MnO_2 in the 3D $Ti_3C_2T_x$@MnO_2 microflowers cathode during electrochemical processes.

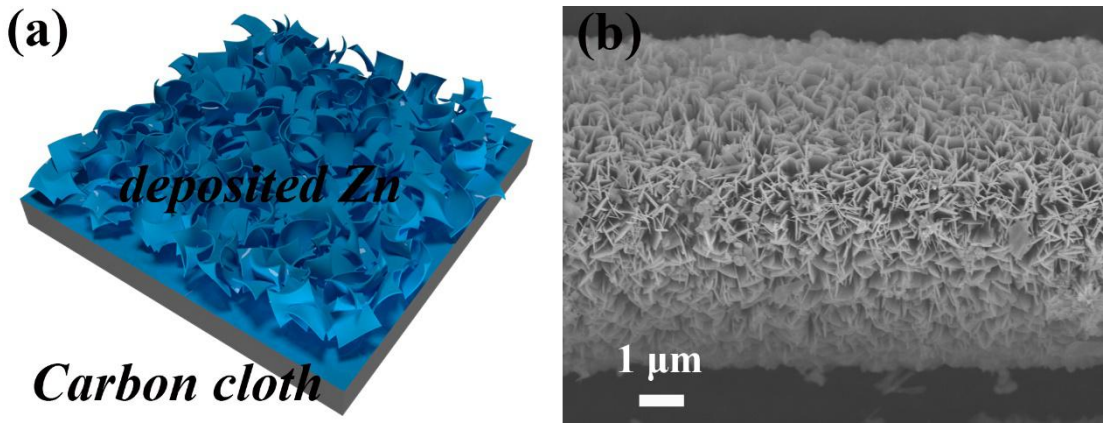

Fig. S17. (a) Sketch map and (b) SEM image of Zn grown on the carbon cloth through electrochemical deposition.

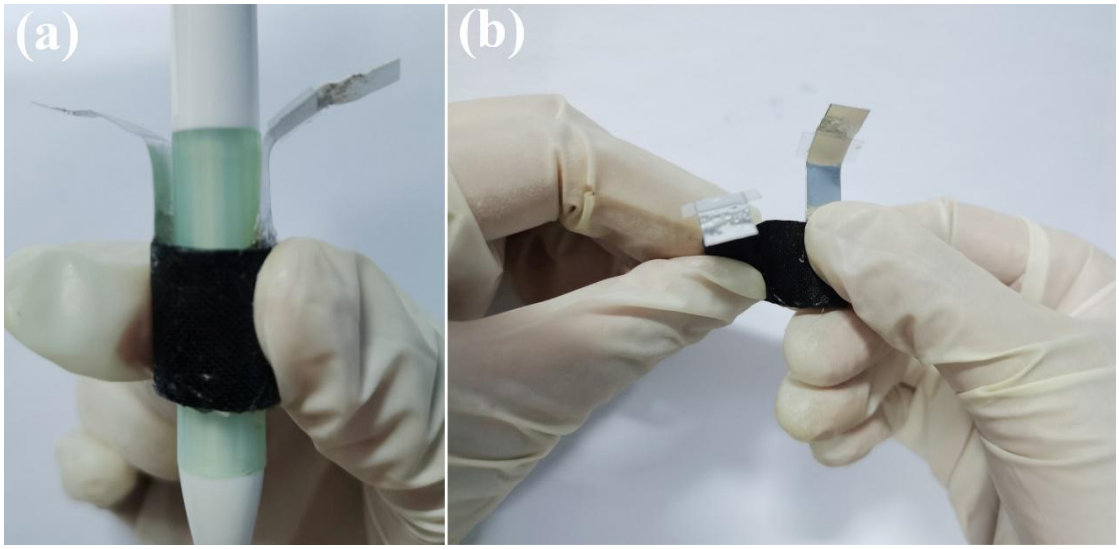

Fig. S18. Digital photos of the flexible aqueous ZIB under (a) bending and (b) twisting states.

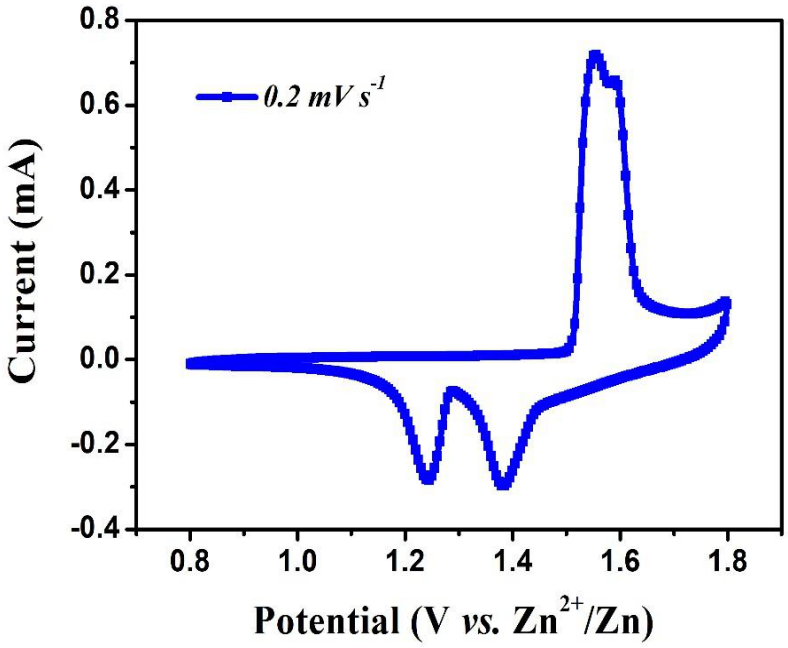

Fig. S19. CV curve of 3D $Ti_3C_2T_x$@MnO_2 microflowers//Zn flexible aqueous ZIBs scaning at 0.2 mV s^{-1}.

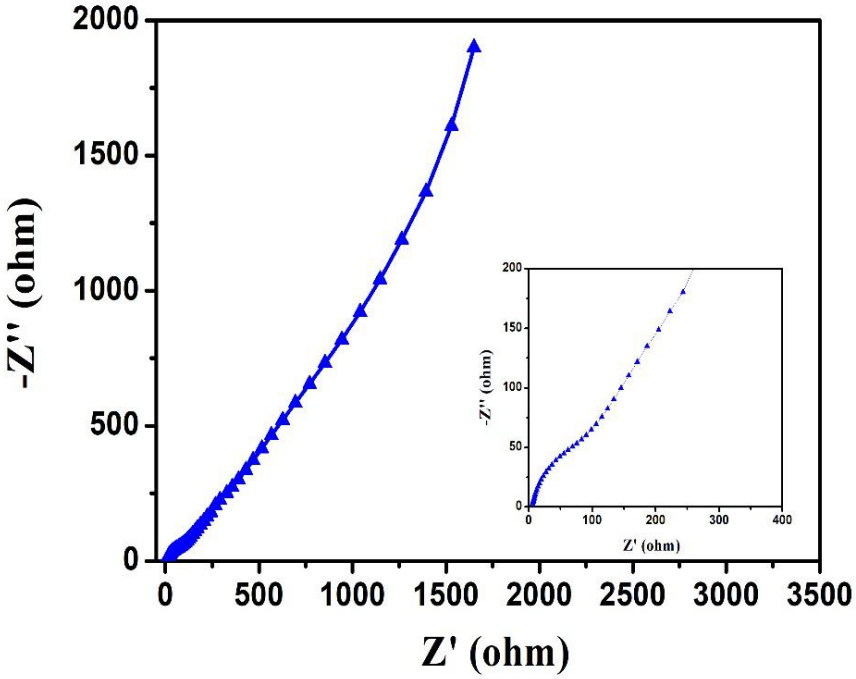

Fig. S20. EIS plot of 3D $Ti_3C_2T_x$@MnO_2 microflowers//Zn flexible aqueous ZIBs.

Table S1. Cycle performance comparisons of 3D $Ti_3C_2T_x$@MnO_2 microflowers cathode with the previously reported MnO_2-based cathode materials for aqueous ZIBs.

Cathode materials	Aqueous electrolyte	Capacity retention	Cycles number	Ref
Amorphous MnO_2	2 M $ZnSO_4$	57.0%	200	[12]
MnO_2 nanorods	1 M $ZnSO_4$	75.0%	200	[13]
La^{3+} intercalated MnO_2	1 M $ZnSO_4$ + 0.4 M $MnSO_4$	71.0%	200	[14]
Birnessite MnO_2	2 M $ZnSO_4$ + 0.5 M $MnSO_4$	61.9%	1500	[15]
Layered MnO_2	1 M $ZnSO_4$	75.3%	200	[16]
β-MnO_2	3 M $ZnSO_4$ + 0.2 M $MnSO_4$	84.3%	1000	[17]
Polyaniline-intercalated MnO_2	1 M $ZnSO_4$ + 0.1 M $MnSO_4$	90.0%	200	[18]
MnO_2@CNT	2 M $ZnSO_4$ + 0.5 M $MnSO_4$	60.0%	100	[19]
MnO_2@graphene	2 M $ZnSO_4$ + 0.4 M $MnSO_4$	64.1%	300	[20]
CNT/MnO_2/PEDOT	2 M $ZnCl_2$ + 0.4 M $MnSO_4$	81.3%	2000	[21]
3D $Ti_3C_2T_x$@MnO_2 microflowers	**2 M $ZnSO_4$ + 0.1 M $MnSO_4$**	**90.6%**	**2000**	**This work**

References

1. Q. Wang, S. L. Wang, X. H. Guo, L. M. Ruan, N. Wei, Y. Ma, J. Y. Li, M. Wang, W. Q. Li and W. Zeng, *Adv. Electron. Mater.,* 2019, **5** 1900537.

2. M. Naguib, O. Mashtalir, M. R. Lukatskaya, B. Dyatkin, C. Zhang, V. Presser, Y. Gogotsi and M. W. Barsoum, *Chem. Commun.,* 2014, **50**, 7420-7423.

3. M. Song, H. Tan, D. Chao and H. J. Fan, *Adv. Funct. Mater.*, 2018, **28**, 1802564.

4. B. Tang, L. Shan, S. Liang and J. Zhou, *Energ. Environ. Sci.*, 2019, **12**, 3288-3304.

5. J. Ming, J. Guo, C. Xia, W. X. Wang and H. N. Alshareef, *Mat. Sci. Eng. R.*, 2019, **135**, 58-84.

6. C. Wang, Y. X. Zeng, X. Xiao, S. J. Wu, G. B. Zhong, K. Q. Xu, Z. F. Wei, W. Su and X. H. Lu, *J. Energy Chem.*, 2020, **43**, 182-187.

7. M. H. Alfaruqi, V. Mathew, J. Gim, S. Kim, J. Song, J. P. Baboo, S. H. Choi and J. Kim, *Chem. Mater.*, 2015, **27**, 3609-3620.

8. Y. L. Zhao, Y. H. Zhu and X. B. Zhang, *InfoMat*, 2020, **2**, 237-260.

9. J. H. Huang, Z. W. Guo, Y. Y. Ma, D. Bin, Y. G. Wang and Y. Y. Xia, *Small Methods*, 2019, **3**, 1800272.

10. G. Z. Fang, C. Y. Zhu, M. H. Chen, J. Zhou, B. Tang, X. X. Cao, X. S. Zheng, A. Q. Pan and S. Q. Liang, *Adv. Funct. Mater.*, 2019, **29**, 1808375.

11. C. Zhan, J. Lu, A. J. Kropf, T. Wu, A. N. Jansen, Y. K. Sun, X. Qiu and K. Amine, *Nat. Commun.,* 2013, **4**, 2437.

12. Y. Wu, J. Fee, Z. Tobin, A. Shirazi-Amin, P. Kerns, S. Dissanayake, A. Mirich and S. L. Suib, *ACS Appl. Energy Mater*., 2020, **3**, 1627-1633.

13. S. Islam, M. H. Alfaruqi, V. Mathew, J. Song, S. Kim, J. Jo, J. P. Baboo, D. T. Pham, D. Y. Putro, Y. K. Sun and J. Kim, *J. Mater. Chem A*, 2017, **5**, 23299-23309.

14. H. Z. Zhang, Q. Y. Liu, J. Wang, K. F. Chen, D. F. Xue, J. Liu and X. H. Lu, *J. Mater. Chem. A*, **7**, 22079-22083.

15. G. Z. Li, Z. X. Huang, J. B. Chen, F. Yao, J. P. Liu, O. L. Li, S.H. Sun and Z. C. Shi, *J. Mater. Chem. A*, 2020, **8**, 1975-1985.

16. K. W. Nam, H. Kim, J. H. Choi and J. W. Choi, *Energ. Environ. Sci*., 2019, **12**, 1999-2009.

17. M. Q. Liu, Q. H. Zhao, H. Liu, J. L. Yang, X. Chen, L. Y. Yang, Y. H. Cui, W. Y. Huang, W. G. Zhao, A. Y. Song, Y. T. Wang, S. X. Ding, Y. L. Song, G. Y. Qian, H. B. Chen and F. Pan, *Nano Energy*, 2019, **64**, 103942-103951.

18. J. H. Huang, Z. Wang, M. Y. Hou, X. L. Dong, Y. Liu, Y. G. Wang and Y. Y. Xia, *Nat. Commun.*, 2018, **9**, 8.

19. L. Zhao, L. B. Dong, W. B. Liu and C. J. Xu, *Chemistryselect*, 2018, **3**, 12661-12665.

20. C. Wang, Y. X. Zeng, X. Xiao, S. J. Wu, G. B. Zhong, K. Q. Xu, Z. F. Wei, W. Su and X. H. Lu, *J. Energy Chem*., 2020, **43**, 182-187.

21. X. Y. Zhang, S. W. Wu, S. J. Deng, W. X. Wu, Y. X. Zeng, X. H. Xia, G. X. Pan, Y. X. Tong and X. H. Lu, *Small Methods*, 2019, **3**, 1900525.